# Oxygen incorporation in aluminum nitride via extended defects: Part I. Refinement of the structural model for the planar inversion domain boundary

Alistair D. Westwood[a)]
*Department of Materials Science and Engineering, Lehigh University, Bethlehem, Pennsylvania 18015*

Robert A. Youngman
*Carborundum Microelectronics Company, 10409 S. 50th Place, Phoenix, Arizona 85044*

Martha R. McCartney
*Center for Solid State Science, Arizona State University, Tempe, Arizona 85287*

Alastair N. Cormack
*New York State College of Ceramics, Alfred University, Alfred, New York 14802*

Michael R. Notis
*Department of Materials Science and Engineering, Lehigh University, Bethlehem, Pennsylvania 18015*

(Received 2 June 1994; accepted 24 January 1995)

The model proposed by Harris *et al.* [J. Mater. Res. **5**, 1763–1773 (1990)], describing planar inversion domain boundaries in aluminum nitride, consists of a basal plane of aluminum atoms octahedrally coordinated with respect to oxygen, and with a translation of $\mathbf{R} = 1/3\langle 10\bar{1}1\rangle + 1/3\langle 0001\rangle$ or $1/3\langle 10\bar{1}\bar{1}\rangle$. This thin sandwich is inserted onto the basal plane of the wurtzite structure of aluminum nitride. This model does not take into consideration any interfacial relaxation phenomena, and is arguably electrically unstable. Therefore, this paper presents a refinement of the model of Harris *et al.*, by incorporating the structural relaxations arising from modifications in local chemistry. The interfacial structure was investigated through the use of conventional transmission electron microscopy, convergent electron diffraction, high resolution transmission electron microscopy, analytical electron microscopy, and atomistic computer simulations. The refined planar inversion domain boundary model is closely based on the original model of Harris *et al.*; however, the local chemistry is changed, with every fourth oxygen being replaced by a nitrogen. Atomistic computer simulation of these defects, using a classical Born model of ionic solids, verified the stability of these defects as arising from the adjustment in the local chemistry. The resulting structural relaxations take the form of a 0.3 mrad twist parallel to the interface, a contraction of the basal planes adjacent to the planar inversion domain boundary, and an expansion of the *c*-axis component of the displacement vector; the new displacement vector across the interface is $\mathbf{R} = 1.3\langle 10\bar{1}0\rangle + \epsilon\langle 0001\rangle$, where $\epsilon_{meas} = 0.387$ and $\epsilon_{calc} = 0.394$.

## I. INTRODUCTION

### A. Background

The presence of extended two-dimensional defects in complex mineralogical systems, tungsten bronzes, mixed tungsten-niobium and tungsten-tantalum oxides, and in rutile has been extensively studied,[1–5] their presence being related to the nonstoichiometry in the material. More recently, extended two-dimensional defects have been reported in aluminum nitride (AlN)[6,7] and zinc oxide (ZnO),[8] both of which possess the wurtzite structure. In AlN, two distinctive morphologies of extended two-dimensional defects are present, a planarvariant and a curved variant which can exhibit three different morphologies: curved, facetted, and corrugated (for a complete discussion of these morphologies, the reader is referred to our second paper, Part II).[9]

This paper will focus on refining the earlier model of Harris *et al.*,[10] for the planar interface structure in AlN, based upon the experimental findings presented here. Our second paper (Part II)[9] will be devoted to understanding the structure and chemistry of the far more complex curved interface, and the formation mechanisms of the planar and curved faults. Finally, the third paper (Part III) will concentrate on a re-evaluation of the high oxygen concentration polytypoid structures in the

[a)]Present address: IBM Research Division, T. J. Watson Research Center, Yorktown Heights, New York 10598.

 

AlN–AlON pseudobinary system. The combined result of these three papers will be an indepth analysis of oxygen incorporation into the wurtzite structure via extended two-dimensional defects and the transformation from a wurtzite-based matrix to a cubic spinel matrix.

The extended planar defect lying on the basal plane {0001} of AlN has received considerable attention from a number of researchers.[6,10–24] This interface has been described variously as an antiphase domain boundary (APB),[15,18] a stacking fault,[6,11,12,20] or as an inversion domain boundary (IDB), which is now known to be the correct structure.[10,16,19,21,22,24]

A correlation between oxygen and the presence of these defects was suggested in many of the studies and was experimentally verified by Westwood and Notis[16] who showed that oxygen was associated with this extended planar defect, and by Youngman *et al.*[17] who showed oxygen to be associated with the curved IDB. This suggests that the extended defects observed in AlN are related to nonstoichiometry, similar to the two-dimensional defects reported in other systems. Interest in the presence of oxygen in AlN, and how it is incorporated in the structure, is heightened because of the detrimental effect that oxygen is known to have on the thermal conductivity of AlN.[25] Westwood and Notis,[16] using convergent beam electron diffraction (CBED),[26] which allows the polarity of the crystals to be determined, showed that the polarity exhibited a 180° reversal across the planar interface. This is indicative of an inversion in symmetry of the crystal structure, identifying this planar extended defect as an IDB. This result was later confirmed independently by Berger[19] and Westwood and Notis,[21] using a conventional transmission electron microscopy (CTEM) multibeam technique.[27] Figure 1 shows the striking contrast reversal on crossing the planar IDB, which is characteristic of an inversion across an interface.

## B. Inversion domain boundaries: Classification and energy

Inversion domain boundaries were first considered by Aminoff and Broome in 1931.[28] An inversion domain boundary relates domain I to domain II by an inversion symmetry operation across the boundary. The lattice is the same on both sides of the boundary, but the structure is inverted. IDB's can occur only in noncentrosymmetric crystals (crystals that do not possess a center of symmetry). The structure of the planar IDB has been categorized into two subtypes: type I was proposed by Austerman and Gehman[29] [see Figs. 2(a), 2(c), and 2(e)], and type II was first put forward by Holt[30] [see Figs. 2(b), 2(d), and 2(f)] even though it was misclassified as an APB. A full explanation behind the confusion that existed in the literature regarding classification of these interfaces as either IDB's or APB's is given by Westwood and Notis.[21] Austerman and Gehman,[29] studying large BeO crystals, proposed that inversion boundaries were present, based upon macroscopic observations of the crystals, etching response, and piezoelectric measurements. They referred to the IDB's as "inversion twins." The inversion twin configuration assumes that the anion sublattice is undeviated across the boundary, with the cation sublattice switching its tetrahedral packing from one set of tetrahedral sites to the other set of tetrahedral sites; see Fig. 2(a). In the case of a fault on a basal plane, the twin is a reflection type (boundary perpendicular to the *c*-axis), while faults on the pyramidal $\{10\bar{1}1\}$ or prism $\{10\bar{1}0\}$ planes are rotation twins (boundary not perpendicular to the *c*-axis); see Figs. 2(c) and 2(e).

Holt[30] introduced the type II IDB configuration consisting of A atoms on A sites and B atoms on B sites in domain I, with A atoms on B sites and B atoms on A sites in domain II [see Figs. 2(b), 2(d), and 2(f)]; note that neither of these two sublattices is continuous across this interface. This type of IDB has been observed experimentally in both SiC[31] and GaAs,[32] epitaxially grown on Si. Across the type II IDB interface, the bonding consists of A-A and/or B-B bonds, of which two types exist, depending upon the interface plane which can either be stoichiometric with equal numbers of A-A and B-B bonds present, or nonstoichiometric with an unequal number of A-A and B-B bonds present across the interface. In the case of boundaries on the basal and pyramidal planes, the bonds are all the same type as shown in Figs. 2(b) and 2(d) (nonstoichiometric), whereas a stoichiometric boundary exists if the habit plane of the IDB is the $\{10\bar{1}0\}$ prism plane, as in Fig. 2(f).

The energy associated with type II IDB interface structures is expected to be considerably greater than type I interfaces because of the "wrong" bonding present across the type II interface. Van Vechten[33] calculated the energy of antistructure pairs (A on a B site, and vice versa) in 23 common compound semiconductors. Using the values quoted in Van Vechten's paper, the energies for type II IDB interface orientations can be estimated based upon the energy of wrong bonds per unit area, and are presented in Table I. From Table I it is understandable why type II IDB's have been observed in GaAs and SiC, but not in AlN or ZnO, because the interfacial energies of the latter compounds are an order of magnitude greater. In the case of the more covalently bonded materials, they attempt to maintain their tetrahedral coordination across the interface,[34] because this situation is energetically more favorable than having a lower coordination and dangling bonds, or too high a coordination and insufficient electrons for bonding, which would occur in a type I IDB interface. Therefore,

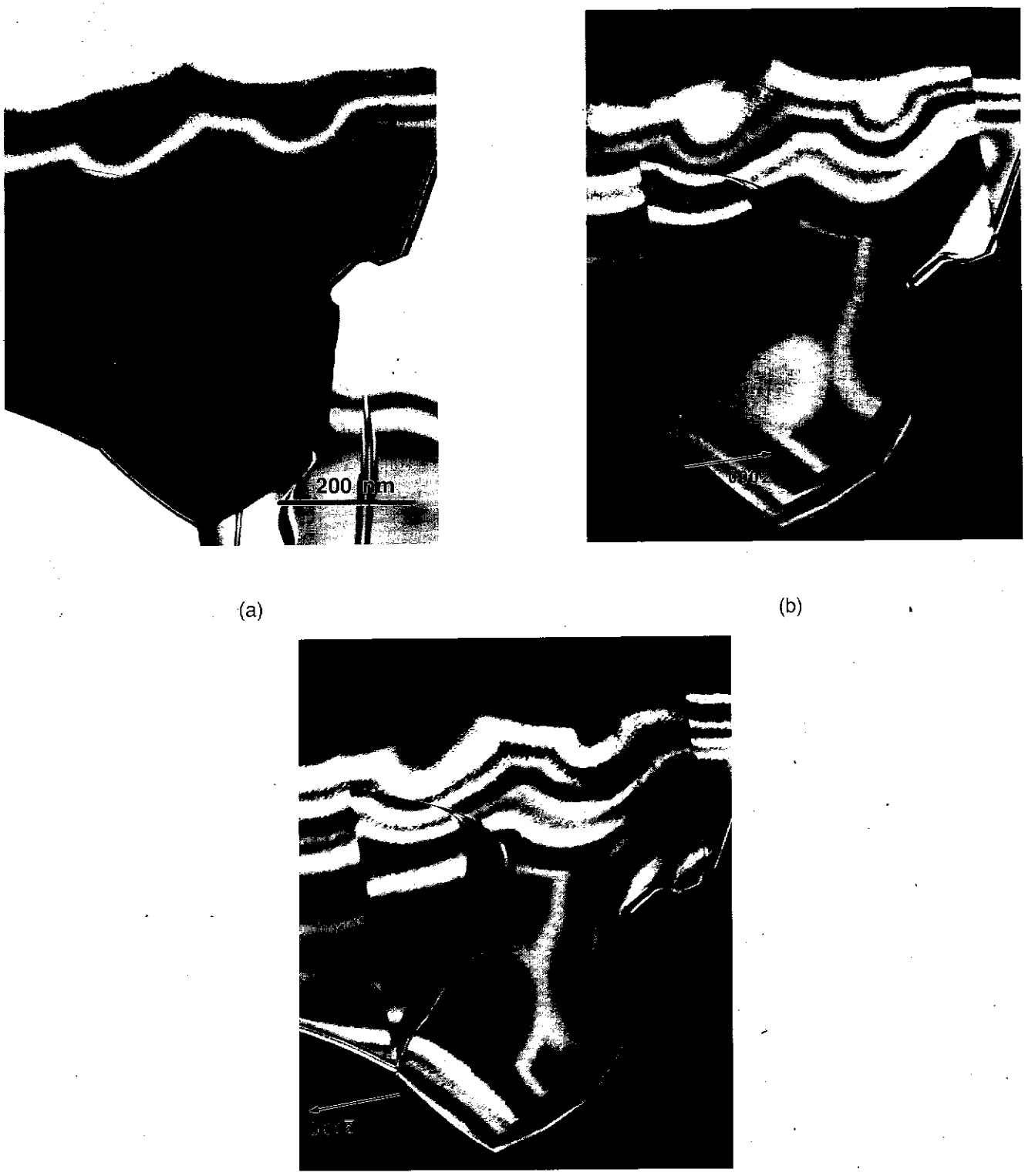


FIG. 1. Bright-field (BF) image of a strongly diffracting grain along a $\langle 11\bar{2}0 \rangle$ zone axis, containing a *D*-shaped IDB (center) and a planar IDB (far right). Note the $\{10\bar{1}1\}$ portion of the curved section of the *D*-shaped IDB at the intersection with the planar IDB. (b) Dark-field (DF) multibeam image using a $g_{(0002)}$ reflection; note the contrast reversal in the thickness fringes across the curved and planar IDB's. (c) A similar image using the $g_{(000\bar{2})}$ reflection; note the contrast is opposite between (b) and (c).

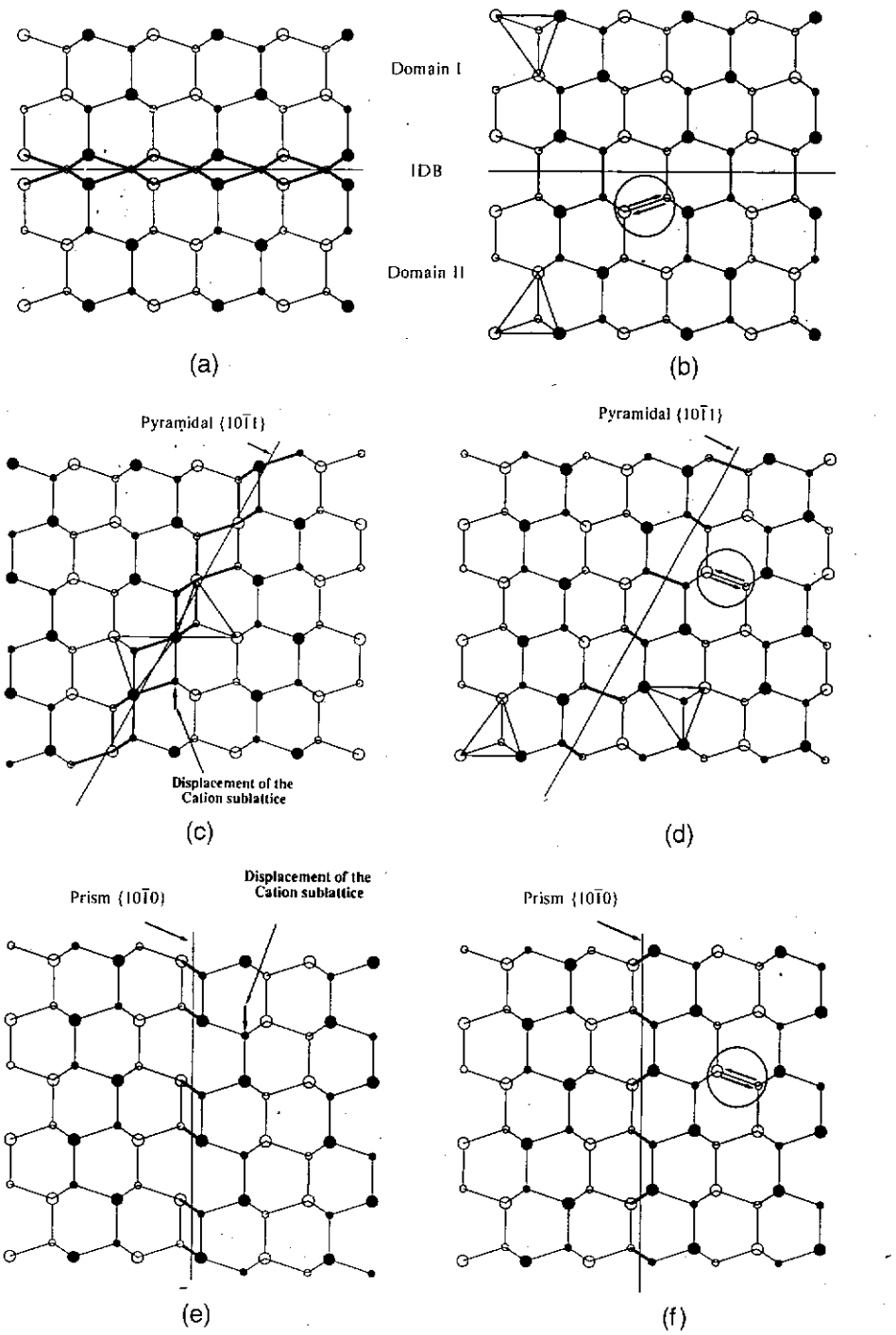


FIG. 2. A schematic showing the two types of inversion boundaries, described here as type I (Austerman and Gehman[29]) and type II (Holt[30]). (a) Type I IDB: cation ion sublattice is undeviated across the interface; cation sublattice switches its tetrahedral site on crossing the interface from domain I to domain II. (b) Type II IDB: cation and anion sublattices have exchanges sites in domain II with respect to domain I. No simple translation can relate domains I and II; therefore, it cannot be an APB. (c) Type I IDB on the polar pyramidal {10$\bar{1}$1}; notice the cation sublattice is continuous across the interface. (d) Type II IDB on the polar pyramidal {10$\bar{1}$1}. (e) Type I IDB on a prism {10$\bar{1}$0}. (f) Type II IDB on a prism {10$\bar{1}$0}. (All schematics are in the ⟨11$\bar{2}$0⟩ projection. Large open circles are nitrogen, small open circles are aluminum, and black circles are a half plane back 1/2 ⟨10$\bar{1}$0⟩).

in covalently bonded materials, wrong bonds may be preferred, rather than the presence of dangling bonds across an interface. In the case of materials possessing a higher ionicity, the presence of wrong bonds will produce large short-range repulsive forces in regions with increased electronic cloud overlap (anions) or in regions with reduced shielding (cations) due to either the acceptance or donation of electrons in other bonding pro-

TABLE I. Calculated interfacial energies for type II IDB interface structures. The calculations are based upon the antisite defect energies calculated by Van Vechten.

| Compound (IDB plane) | IDB energy ($Jm^{-2}$) |
|---|---|
| SiC(110) | 2.1 |
| GaAs(110) | 1.0 |
| AlN(0001) | 12.9 |
| ZnO(0001) | 26.6 |

cesses with nearest neighbors. Therefore, ionic materials are expected to prefer type I IDB interfaces, avoiding the short-range repulsive forces related to the wrong bonding across the type II IDB interface. However, the tetrahedral coordination present in wurtzite or sphalerite structures cannot be maintained across a type I interface. Therefore, for an inversion to exist across an interface in these structures, the coordination must be either twofold or sixfold, or more, and deviation from the ideal coordination will contribute toward the interfacial energy of the IDB. Unfortunately, no energy calculations for type I IDB interfaces are available.

The only known calculations for interfacial energies of IDB's rather than just the estimates based upon Van Vechten's approach, were carried out by Lambrecht and Segall.[35] They calculated the energy for an unrelaxed type II IDB in SiC on the (110) planes as $\simeq$7.3 $Jm^{-2}$ (compared to 2.1 $Jm^{-2}$ based upon the values of Van Vechten). Because of the high energy associated with these IDB interfaces, relaxation will likely take place. A number of processes are available to allow the interface to reduce its energy, even though it may be constrained by the bulk crystal structures. These processes, collectively known as relaxation processes, can be arranged into five groups: line (dislocations), rigid body translations, segregation, facetting, and interfacial expansion or contraction.[36] Lambrecht and Segall[35] calculated the relaxed energy of a SiC(110) type II IDB as $\simeq$3.65 $Jm^{-2}$, which is half of the unrelaxed energy. Interfacial relaxation can produce large changes in interfacial energy, in excess of two orders of magnitude.[37] The mode of relaxation at the SiC(110) type II IDB was described by Lambrecht and Segall[35] as bond rotation of the Si–C bonds. In their model they proposed that the Si atoms move farther apart and the C atoms approach each other. The energy of the relaxed IDB in SiC compares favorably with calculated grain boundary energies for a number of ceramic oxides.[38,39] These calculated energies, for a number of different orientations, lie between $\simeq$0.5 and 3.5 $Jm^{-2}$. This comparison appears to indicate that these (110) type II IDB's should not occur in the material, but rather, grain boundaries should form. However, carbide grain boundary energies may be significantly higher than oxide grain boundary energies, because a covalent solid would try to maintain tetrahedral coordination across the boundary, which could cause large distortions within the surrounding lattice. This may result in the grain boundary energy being much higher than the IDB energy, and thus the IDB structure would be preferred. No information is available on the measured or calculated energies of carbide grain boundaries.

Kim and Goo,[8] studying a planar IDB in wurtzite ZnO, determined it to have a type I configuration, comprised of a basal plane of oxygen atoms which are at the intersection of the apices of two inverted tetrahedra, a basal plane translation, and a contraction in the *c*-axis. In this configuration, the oxygen atom is bonded to only two zinc atoms, 180° apart, rather than the normal four zinc atoms in tetrahedral coordination. Based upon Pauling's electrostatic valence principle,[40] one would expect that this IDB structure would be highly unstable, suggesting that the proposed IDB structure of Kim and Goo may not be appropriate.

From our studies on AlN, it appears that "pure" type I and type II IDB structures—similar to those suggested for ZnO,[8] GaAs,[32] and SiC[31] and used in the calculations of Lambrecht and Segall[35]—are unstable. In AlN the formation of IDB's is known to be strongly related to oxygen, which is incorporated as an impurity.[10,14,16,17,21–24] the possibility therefore exists that the presence of IDB's in other materials may likewise be related to low concentration impurity effects. Supporting evidence for this comes from recent work by Makovec and Trontelj,[41] who showed titanium segregation to IDB structures in $Bi_4Ti_3O_{12}$ doped ZnO, and by Bruley *et al.*,[42] whose work indicated the segregation of antimony to the planar IDB in $Sb_2O_3$-doped ZnO. In the proposed model of Kim and Goo,[8] and the calculations of Lambrecht and Segall,[35] they have both neglected to consider the effects of impurities on the formation of IDB's. The varistor material of Kim and Goo[43] contained 2 wt. % $Bi_2O_3$, 1 wt. % $Sb_2O_3$, 1 wt. % $MnCO_3$, and 1 wt. % CoO; and in SiC, both B and C are added as sintering aids. The formation of these IDB structures may be a simple method for removing the nonstoichiometry present in the lattice as a result of the presence of impurities. It is suggested that these impurities may thus allow the stabilization and formation of low energy interfaces, and this appears to be occurring in AlN.

### C. Structural models of the extended planar defect in aluminum nitride

A number of structural models have been proposed to describe the oxygen-containing extended planar defects present in AlN. Hagege *et al.*[6,11,12] and Hagege and Ishida[20] have suggested a number of different interface models, all consisting of a stacking fault centered on a nitrogen-oxygen basal plane which was octahedrally

coordinated to aluminum, each model differing by the magnitude of the displacement vector, McKernan and Carter[15] initially suggested that the interface was an APB, and was comprised of 1/2 unit cell of alumina. McKernan *et al.*[18] later reappraised their work, proposing a similar APB model, but based on 1/3 of a unit cell of alumina. Although not initially proposing a structural model, Westwood and Notis[16] identified these defects as IDB's, making the above two models (stacking faults and APB's) incorrect. This work has since been supported by Berger,[19] Massler *et al.*[44] and Westwood and Notis.[21] Harris *et al.*[10] proposed a defect model emphasizing a logical sequence of oxygen incorporation: initially as a substitutional impurity on the nitrogen sublattice and associated with an aluminum vacancy; continued oxygen incorporation produces an octahedral defect, in which an aluminum atom was octahedrally coordinated to six oxygen atoms; at increased oxygen concentrations, these octahedral defects coalesce to form an extended planar IDB. This model is consistent with the expected structural rearrangement when oxygen comes into contact with tetrahedrally coordinated aluminum based upon Pauling's rules. Their proposed model of the IDB possesses a displacement vector $\mathbf{R} = 1/3\langle 10\bar{1}1\rangle$, which can be split into the two perpendicular components $\mathbf{R} = 1/3\langle 10\bar{1}0\rangle + 1/3\langle 0001\rangle$.

Strong supporting evidence in favor of the model proposed by Harris *et al.*[10] came from two independent techniques: high-resolution transmission electron microscopy (HRTEM) with quantitative image simulations,[23] and quantitative analytical electron microscopy (AEM) with Monte Carlo x-ray generation simulations.[22,24] During the HRTEM studies, asymmetry was observed in the structure image obtained from either side of the planar IDB. This was attributed to a small twist parallel to the planar IDB, and whose axis was parallel to the $\langle 0001\rangle$. In addition, based upon charge neutrality arguments, Youngman[45] suggested that every fourth oxygen in the two adjacent oxygen basal planes be replaced by a nitrogen. The presence of three nitrogen atoms for every two octahedral defect units will cause distortion of the ideal octahedral configuration of aluminum and oxygen. The introduction of the nitrogen at the interface is likely to cause relaxation of the interface, which is apparent from the presence of the twist, and will produce changes in the rigid body translation at the interface. The original displacement vector $\mathbf{R} = 1/3\langle 10\bar{1}1\rangle$ was proposed for the perfect octahedral configuration; however, the presence of nitrogen distorts the ideal octahedral coordination, and thus a different displacement vector will be required to describe the interface.

With these relaxation effects in mind, the planar IDB has been re-examined with the aim of refining the model both structurally and chemically using CTEM, HRTEM, AEM, CBED, and atomistic calculations. These atomistic calculations are the first reported attempt at determining the energy of a type I IDB interface.

## II. EXPERIMENTAL PROCEDURE

### A. Sample preparation

The AlN samples used in this study were fabricated from commercially available AlN powder (Tokuyama Grade F) containing $\simeq$1 wt.% oxygen, cation impurities totaling <370 ppm (220 ppm C, 98 ppm Ca, 37 ppm Si, 10 ppm Fe), and with an average particle size of $\simeq 1\ \mu$m. Powder processing was conducted in a dry box, in which the moisture content was maintained below 10 ppm $H_2O$, minimizing further oxygen pickup during processing. The samples were fabricated by hot pressing in a graphite die coated with boron nitride (BN). The hot pressing conditions were 1800 °C, a 20 MPa load, for 1 h, in a $N_2$ atmosphere.

The samples used for electron microscopy studies were prepared by cutting thin slices from the fabricated bulk samples using a diamond saw, followed by ultrasonically cutting 3 mm disks out of the slices. These disks were then dimpled to a final thickness of $\simeq 10$–$20\ \mu$m. The sample was ion beam thinned to perforation using 4 kV Ar ions at a grazing incident angle of 10°–12°.

### B. Instrumentation

CTEM and CBED were conducted on a Philips 400T microscope equipped with a $LaB_6$ electron source and operated at 120 kV. The large range of $C_2$ apertures, the variable voltage control, and the ±45° tilt goniometer specimen stage made this an ideal instrument for CBED. During some of the convergent beam analyses, the sample was cooled to −186 °C using a cooling stage, a method that reduced thermal lattice vibration and therefore improved image quality.

HRTEM was conducted on a JEOL JEM-4000EX microscope fitted with a $LaB_6$ filament and operated at 400 kV. The use of the high resolution top-entry double-tilt specimen stage allowed ±20° of tilt. The optical parameters of the microscope used in image simulation calculations were spherical aberration constant, $C_s$ = 1.00 mm, beam convergence semiangle ($\alpha$) = 0.5 mrad, and an electron beam focal spread ($\Delta f$) = 8.0 nm. The interpretable resolution of this microscope at Scherzer defocus (−49.7 nm) was 0.17 nm.

The HRTEM image simulations of the defect models were generated using a multislice algorithm in the EMS V3.2 program.[46] Three supercells were created in the $\langle 11\bar{2}0\rangle$ projection, one based on the experimental results, and two based on the equilibrium structure predicted by the atomistic simulations. These supercells differed only in their $a$-axis values; the experimental supercell dimensions were $a$ = 5.6106 nm, $b$ = 0.5388 nm,

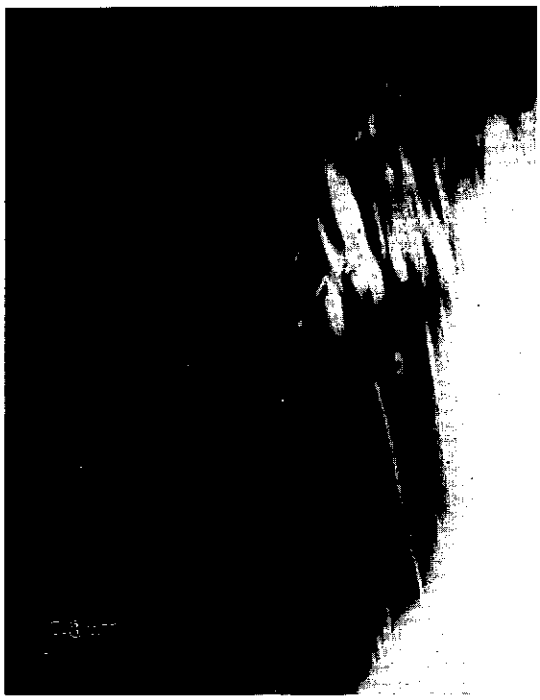

(a)

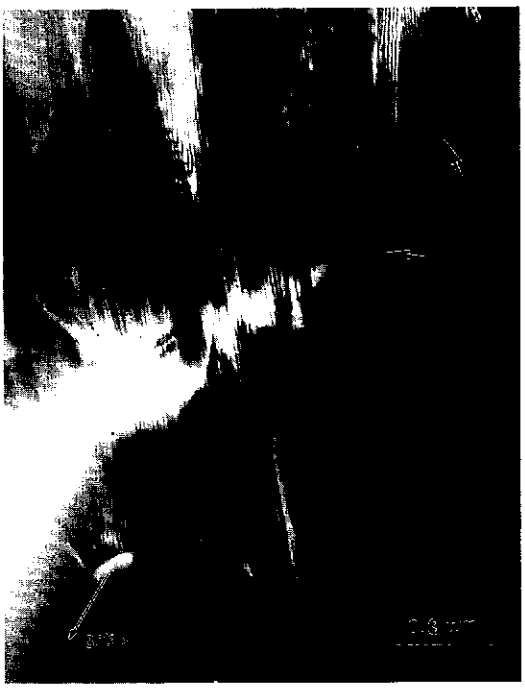

(b)

FIG. 3. (a) BF image of a series of planar and curved IDB's; (b) a DF image obtained using a $g_{(30\bar{3}3)}$ reflection; fringe contrast is clearly present for both curved and planar IDB's (arrowed). If the displacement vector $\mathbf{R} = 1/3\langle 10\bar{1}1\rangle$ as proposed by Harris *et al.*[10] was correct, no fringe contrast should have been observed.

and $c = 0.3111$ nm, and the atomistic supercell dimensions were $a = 5.5272$ nm, $b = 0.5388$ nm, and $c = 0.3111$ nm, and $a = 5.3529$ nm, $b = 0.5388$ nm, and $c = 0.3111$ nm. The supercells each contained 86 atoms. For further details regarding the Debye–Waller factors, scattering factors, "aliasing" effects, and processing of experimental and simulated images, the authors refer the reader to McCartney *et al.*[23] Analytical electron microscopy (AEM) was conducted using a Vacuum generators HB-501 dedicated scanning transmission electron microscope (STEM) equipped with a cold-field emission gun (FEG) source, in an ultrahigh vacuum ($1 \times 10^{-9}$ Torr), and operated at 100 kV. In all analyses, a probe size of 1.0 nm full-width half-maximum (FWHM) and 1.8 nm full-width tenth-maximum (FWTM)[47] was employed with a probe current of $0.2–0.4 \times 10^{-9}$ A. Fitted to the HB-501 was a Link windowless Si(Li) detector with an active area of 30 mm$^2$, a collection angle of 0.077 sr, and an energy resolution of $\simeq$140 eV at Mn $K_\alpha$, and was capable of detecting elements with $Z > 4$. The HB-501 was also fitted with a Link serial electron energy loss spectrometer, which was used for determining the sample thickness.[48]

### C. Atomistic computer simulations

Computer simulation of atomic structures and processes has become a well-established technique for the analysis and modeling of a wide variety of solid-state physics problems.[49] The aim of all atomistic computer simulations is to describe as accurately as possible the interactions among the electrons and atomic nuclei of the material under investigation, since it is these interactions that ultimately control the bonding and properties of the material.

There are two different simulation methodologies: static lattice (either perfect or defect) or molecular dynamics. The choice of the simulation methodology is governed to some degree by the material and the properties of interest. In this work, static lattice simulations, including energy minimization equilibration procedures, were used.

One of the most common problems employing computer simulations is the study of crystallographic lattice defects, and this is true in this paper. The benefit of atomistic computer simulation to this problem is the level at which the analysis can be carried out, since the structure and chemistry of individual atoms at the defect can be studied in a very precise and controlled manner. An additional advantage of simulation procedures is that they allow the study of a wide variety of different defect chemistries and structures, enabling trends to be analyzed far more easily than if the compounds had to be fabricated from the raw materials. The programs are sufficiently well advanced to predict the structures of compounds not yet studied, given appropriate potential models. Central to all simulation procedures is the need for an accurate representation of the interatomic forces

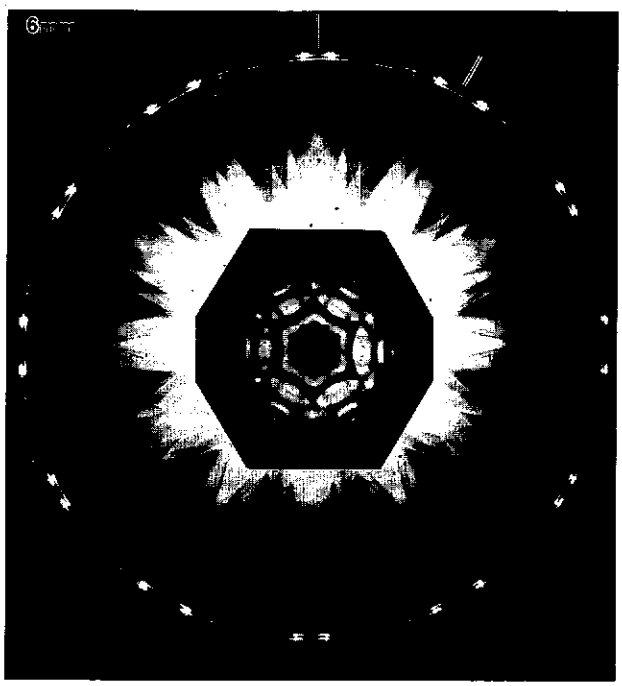


(a)

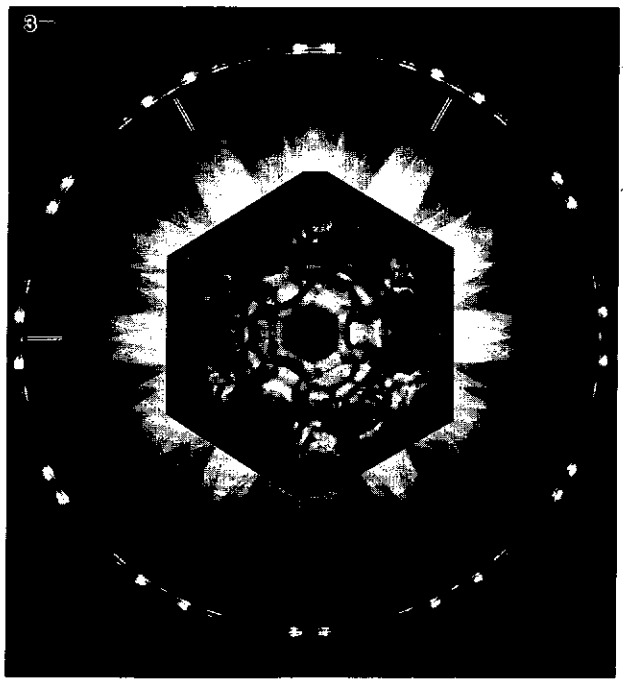


(b)

FIG. 4. (a) CBED pattern ⟨0001⟩ from the matrix adjacent to the planar IDB, 6 mm symmetry, and (b) CBED pattern ⟨0001⟩ obtained when the probe was positioned on the planar IDB, 3 m symmetry. The bars indicate the mirror planes.

in the material. Classically, a parameterized interatomic potential model is employed. These models are the most widely used in atomistic simulations, especially for complex systems such as are dealt with here, although *ab initio* methods are becoming more common as computer power increases.

In this work the model of Cormack[50] is used, employing pair potentials to describe the atomic interactions and model the behavior of pure defect-free AlN. The computer simulation treats the structure as an ionic solid. Although the original program was developed for ionic solids, it has since been modified by the inclusion of a directional bonding component, which allows more accurate simulations of covalently bonded structures. However, Cormack,[50] studying AlN (44% ionic component based upon the ionicity scale of Philips[51] and Van Vechten[52] using the dielectric definition of electronegativity), showed that AlN did not require the directional bonding component because it behaved more like an ionic material due to charge localization around the ions. This observation decreased the complexity of the calculation since we could discard the directional bonding portion of the calculation. The interatomic potentials describing the attractive (Madelung potential, van der Waals, zero point terms) and repulsive (electron cloud interactions) forces between identical and different atomic species must first be determined. The accuracy with which the interatomic potential is known will determine the accuracy of the simulation. The interatomic potentials can be determined *ab initio*,[53] or empirically by fitting the calculated values of the lattice parameter,


FIG. 5. A weak-beam image using a $g_{(1\bar{1}01)}$ of the planar IDB interface showing the regular displacements of the fringe contrast of the fault at the locations where the extinction contours intersect the fault.

bulk modulus, and high and low frequency dielectric properties with that of the experimentally determined crystal properties.[50,54] The interatomic potentials are adjusted until a best fit is obtained between the experimental and calculated values. The best fit is based upon the minimization forces between the atoms, i.e., equilibrium when zero forces (strains) on all atoms.

The program requires as input the trial atomic coordinates of each ion in the supercell of interest (the structural cell which contains the defect), the interatomic potentials between all of the different species in the supercell, the charge on the ions, and the supercell lattice parameters. The program uses a well-tested algorithm to sum up the attractive and repulsive elements of all the interatomic potentials used, to thus obtain the cohesive energy or lattice energy per mole of the solid.[55–57] Energy minimization is used to find an equilibrium structure, a procedure which includes relaxation effects which are known to be an important aspect in stabilizing extended defect structures.[50,58] Unfortunately, it was difficult to compare directly two different defect types due to the nature of the input supercell,[59] and to determine the actual interfacial energy of the defect. However, within the spectrum of different defect structures, trends and relative stabilities could be calculated and compared. This was achieved by calculating the theoretical energy of the system based upon the constituents (number of moles of AlN, number of oxygen atoms sitting on nitrogen sites, and the number of aluminum vacancies); this theoretical energy was subtracted from the calculated energy of the (relaxed) system to give $\Delta E$, values which are discussed later in Sec. III.D. The difference is a measure of the stability, with more stable structures being indicated by larger (negative) energy differences. All computations were carried out on a VAX computer.

## III. OBSERVATIONS AND RESULTS

### A. Conventional transmission electron microscopy (CTEM)

The initial objective was to determine if the displacement vector $\mathbf{R} = 1/3\langle 10\bar{1}1\rangle$ of the Harris *et al.*[10] model was correct. If so, only the relaxation related to the twist need be determined. The CTEM two-beam invisibility criterion was used to verify the displacement vector. The criteria for determination of the displacement vector $\mathbf{R} = 1/3\langle 10\bar{1}1\rangle$ reveal that under four of the twelve possible $\{10\bar{1}1\}$ type reflections, and for all twelve $\{30\bar{3}3\}$ reflections, the planar interface should be invisible when viewed using one of the above reflections, assuming that the displacement vector $\mathbf{R} = 1/3\langle 10\bar{1}1\rangle$ was correct. Figure 3 shows that the planar IDB's clearly produce fringe contrast when imaged using a $g_{(3033)}$ reflection. The presence of the fringe contrast indicates that the original choice of the displacement vector required adjustment. The displacement vector in a hexagonal crystal structure can be separated into two perpendicular components: one in the basal plane and the second along the $c$-axis, e.g., $\mathbf{R} = 1/3\langle 10\bar{1}0\rangle + 1/3\langle 0001\rangle$. Therefore, three possibilities may account for the change in the displacement vector: a relaxation causing a change only in the basal plane displacement, only a change in the $c$-axis displacement, or a relaxation which produces a change in both components of the displacement vector. A further problem was noticed in the two-beam analysis; the number and contrast of the fringes were very sensitive to small deviations in $s$ (the deviation from the exact Bragg diffraction condition), making image interpretation more difficult.

CBED patterns obtained along the $\langle 0001\rangle$ zone axis confirmed the presence of $1/3\langle 10\bar{1}0\rangle$ translation. Figure 4(a) shows a CBED pattern obtained from the matrix, and possessing the characteristic $6mm$ symmetry of the wurtzite structure. Figure 4(b) shows a CBED pattern obtained form the region of the planar IDB; the pattern displays $3m$ symmetry. This symmetry reduction ($6mm \rightarrow 3m$) is consistent with the $1/3\langle 10\bar{1}0\rangle$ translation. Therefore, the relaxation of the displacement vector had to be in the $c$-axis displacement. A number of different two-beam conditions were tried in an attempt to determine the magnitude of the $c$-axis displacement. The results were inconclusive, indicating that the magnitude was not a simple fraction of a lattice vector.

A weak-beam technique developed by Miyazawa and Ishida,[60] and Miyazawa *et al.*[61] allows the determination of displacement vectors that need not be described by whole fractions. The technique requires imaging the interface under a weak-beam condition, with $3g$ excited.[62] Under these conditions a displacement of the planar interface fringe contrast occurs with respect to the extinction contours, due to the presence of a displacement at the interface. The relative displacement ($\Delta n$) in the fringe contrast of the planar defect, with respect to the extinction contours, can be directly measured from the weak-beam image; see Fig. 5. The technique relies upon the relationship $\mathbf{g} \cdot \mathbf{R} = \Delta n + s$ and the ability to obtain the shift for a number of different reflections. The value of $s$ is considered positive if the interface fringe contrast is displacement toward the foil edge, and negative if displaced away from the foil edge; the value of $\Delta n$ must lie between $-1/2 < \Delta n < 1/2$.

Because the basal plane component of the displacement vector is known, the $c$-axis component could be isolated by using the appropriate operating reflection; $g_{(1101)}$ was used. This enables the effect of the basal plane component on the relative shift of the fringe contrast to be calculated separately; the difference between the measured displacement and the calculated basal plane displacement is attributable to the $c$-axis

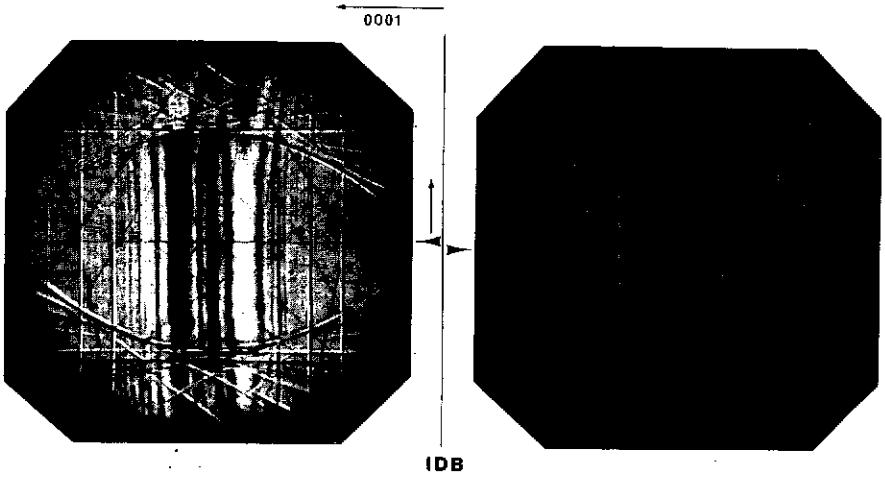


FIG. 6. Scanning transmission electron microscopy (STEM) CBED patterns taken along the $\langle 2\bar{2}01\rangle$ zone axis from either side of a planar IDB. The arrows indicate a small shift in the HOLZ lines in the direction indicated which is parallel to the interface. The translation corresponds to a small crystal tilt which is a small 0.3 mrad rotation parallel to the interface, with the rotation being along the $\langle 0001\rangle$.

displacement. Using this approach the *c*-axis displacement was found to be $-0.113\langle 0001\rangle \pm 0.5\langle 0001\rangle$. Because no observable difference would be seen with a displacement of $0.5\langle 0001\rangle$, the displacement can be expressed as a positive quantity $0.5\langle 0001\rangle - 0.113\langle 0001\rangle = 0.387\langle 0001\rangle$.

Quantitative analysis using the weak-beam technique requires comparison between the experimentally obtained image and a simulation of the fringe contrast. The input requirements for the simulated image are the experimentally determined displacement vector and the diffraction conditions ($g$ and $s$) under which the experimental image was obtained. Unfortunately, the fringe contrast simulation programs[63,64] cannot incorporate the crystal potential change at the interface due to the presence of oxygen (see Ref. 9, Part II for a full explanation); therefore, the experimentally determined displacement vector could not be verified by image simulation. Therefore, the displacement vector measured using the weak-beam technique could not be quantified through matching of experimental and simulated images.

The twist present across the interface was measured from the shift in the higher order Laue zone (HOLZ) lines in the CBED patterns from either side of the interface. The shift in the HOLZ lines can be seen in the STEM CBED pattern in Fig. 6. This shift reflects a tilt of one crystal relative to the other, and was measured to be $\simeq 0.3$ mrad. This tilt corresponds to a twist of a similar magnitude parallel to the interface, with the twist axis being parallel to the $\langle 0001\rangle$.

## B. High-resolution transmission electron microscopy

Because of the problem in quantifying the revised *c*-axis component of the displacement vector using the weak-beam technique, HRTEM was used with the hope that the displacement vector could be obtained from the image simulations. Figure 7 shows an HRTEM image of the planar IDB viewed along $\langle 11\bar{2}0\rangle$; under these viewing conditions, the dark lozenge shapes are the Al–N pairs. The image of the planar IDB is identical to that of McCartney *et al.*[23] McCartney *et al.* had used

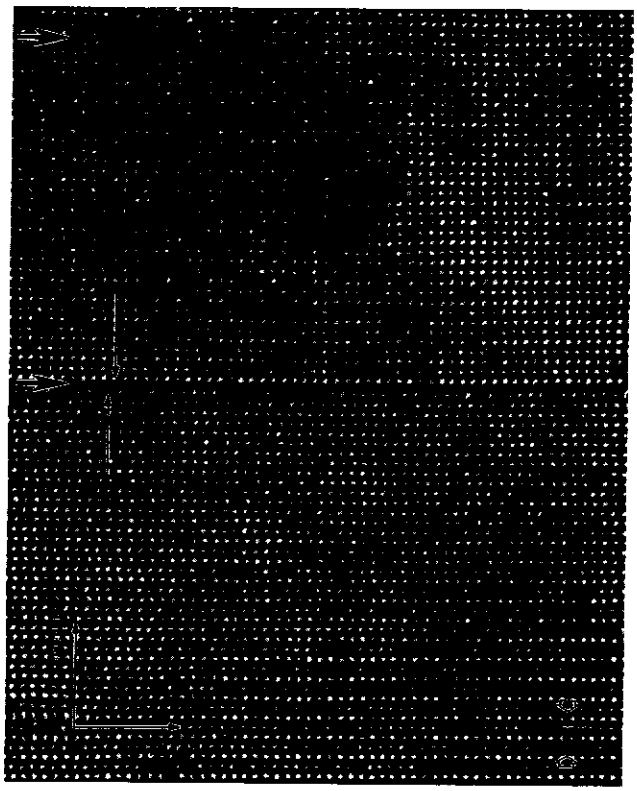

FIG. 7. A HRTEM image of the planar IDB interface viewed along the $\langle 11\bar{2}0\rangle$. The basal plane translation of $1/3\langle 10\bar{1}0\rangle$ can be seen, and the black lozenge shapes between the white dots represent Al–N pairs.

the original displacement vector of Harris *et al.*[10] in their image simulations. The same basic model was used for the image simulations in this paper, except that the *c*-axis displacement was adjusted from the original values of $0.333\langle 0001\rangle$ to $0.387\langle 0001\rangle$, to match the experimentally measured weak-beam value. The $1/3\langle 10\bar{1}0\rangle$ basal plane translation was retained, based upon the CBED results.

The image simulations were carried out for various defocii and thicknesses, with a reasonable match being obtained between the experimental and the simulated image, as shown in Fig. 8. However, the simulated image appears to be slightly too large, with basal planes on one side of the boundary being misaligned. This was also observed in the model of Harris *et al.*, but to a lesser degree.[23] Comparison between the HRTEM image simulations obtained in the present study and those obtained by McCartney *et al.*,[23] based upon the model of Harris *et al.*,[10] indicates that no difference could be seen in the image characteristics of the two simulations over a wide range of defocii and thicknesses; see Figs. 9(a) and 9(b). According to Saxton and Smith,[65] it is possible to determine atomic positions using HRTEM to within 14 pm (0.014 nm); this requires a through-focal series reconstruction of the experimental images. In the present case, the difference in *c*-axis displacement vector components, $0.333\langle 0001\rangle$ and $0.387\langle 0001\rangle$, corresponds to 26 pm (0.026 nm). This is near the limit of atomic position determination using HRTEM, as suggested by Saxton and Smith.[65] Therefore, it appears that it is not possible to determine unambiguously the small differences between these two models using HRTEM.

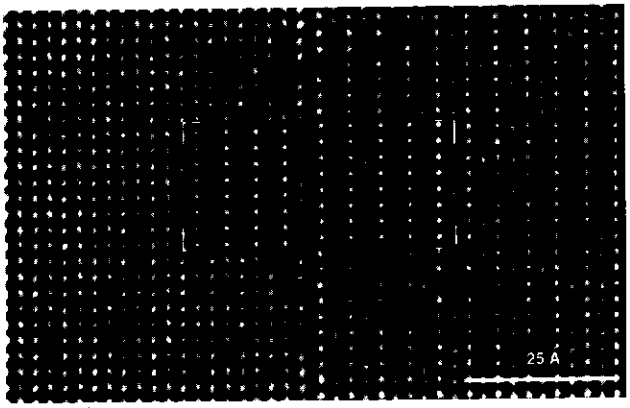


FIG. 8. A HRTEM image of the interface with a simulated image based upon the refined planar IDB model with the adjusted *c*-axis displacement vector, $\mathbf{R} = 1/3\langle 10\bar{1}0\rangle + 0.387\langle 0001\rangle$. A reasonable match is obtained between the experimental and simulated images. The width of the fault appears to be too large, and also a slight misregistry can be seen in the atomic planes on the right-hand side of the IDB. (Simulated image: $\Delta f = -43.7$ nm, at a foil thickness of 4.5 nm.)

### C. Analytical electron microscopy (AEM)

For a full account of the experimental AEM work, the authors refer the reader to Westwood *et al.*[22,24] The oxygen concentration profiles obtained across the planar IDB are presented in Figs. 10(a) and 10(b). In each case, oxygen segregation was found to be limited within a very narrow region, with maximum concentrations of $6.5 \pm 0.9$ wt.% [Fig. 10(a)], and $6.0 \pm 0.8$ wt.% [Fig. 10(b)]. Both these profiles were obtained from different IDB's in a region 110 nm thick. There appears to be an oxygen-depleted region extending out to 20 nm on either side of the IDB. The matrix oxygen concentration on either side of the IDB appears to be asymmetric once outside of the oxygen-depleted zone. At random locations along the IDB, small amounts of calcium were detected; calcium is an impurity present in the starting AlN powder. When a number of other data points that were not part of the profile were taken from locations along the IDB interface, they revealed small fluctuations in the oxygen concentration. Table II provides all the experimentally determined oxygen concentration data obtained from points on the planar IDB's. The variance present in the oxygen concentrations obtained from different locations along the IDB's may be due to counting statistics, because the oxygen peak generally contained only 1500–2000 counts.

The aluminum, nitrogen, and oxygen profiles for the IDB shown in Fig. 10(a) are seen in Fig. 11. The nitrogen concentrations appear to decrease at the boundary, whereas the aluminum concentration appears to be undeviated. This result would be expected, because in all the models oxygen is replacing nitrogen on the nitrogen sublattice in the AlN structure with the aluminum sublattice unaffected.

Monte Carlo electron trajectory simulations[66] treat the interface (the IDB) as a plate-like precipitate running through the foil thickness, with the precipitate oriented parallel to the electron beam. The input to the program required the assumed IDB composition and density based upon the proposed models, the specimen thickness, the density and composition of the matrix in which the precipitate was sitting, the electron probe size, and the number of electron trajectories. Eight different IDB models were chosen for simulation based upon their structure and associated chemistry; the various models had been proposed by Hagege *et al.*,[12] Hagege and Ishida,[20] McKernan *et al.*,[18] Harris *et al.*,[10] McCartney *et al.*,[23] Youngman,[45] and Westwood[59]; see Table III. The Monte Carlo simulation program[67] was executed on a massively paralleled computer, the advantage being the extreme speed of operation allowing far more trajectories to be simulated, improving statistical accuracy. To improve the simulation it was assumed that the AlN matrix contained $\simeq 1$ wt.%

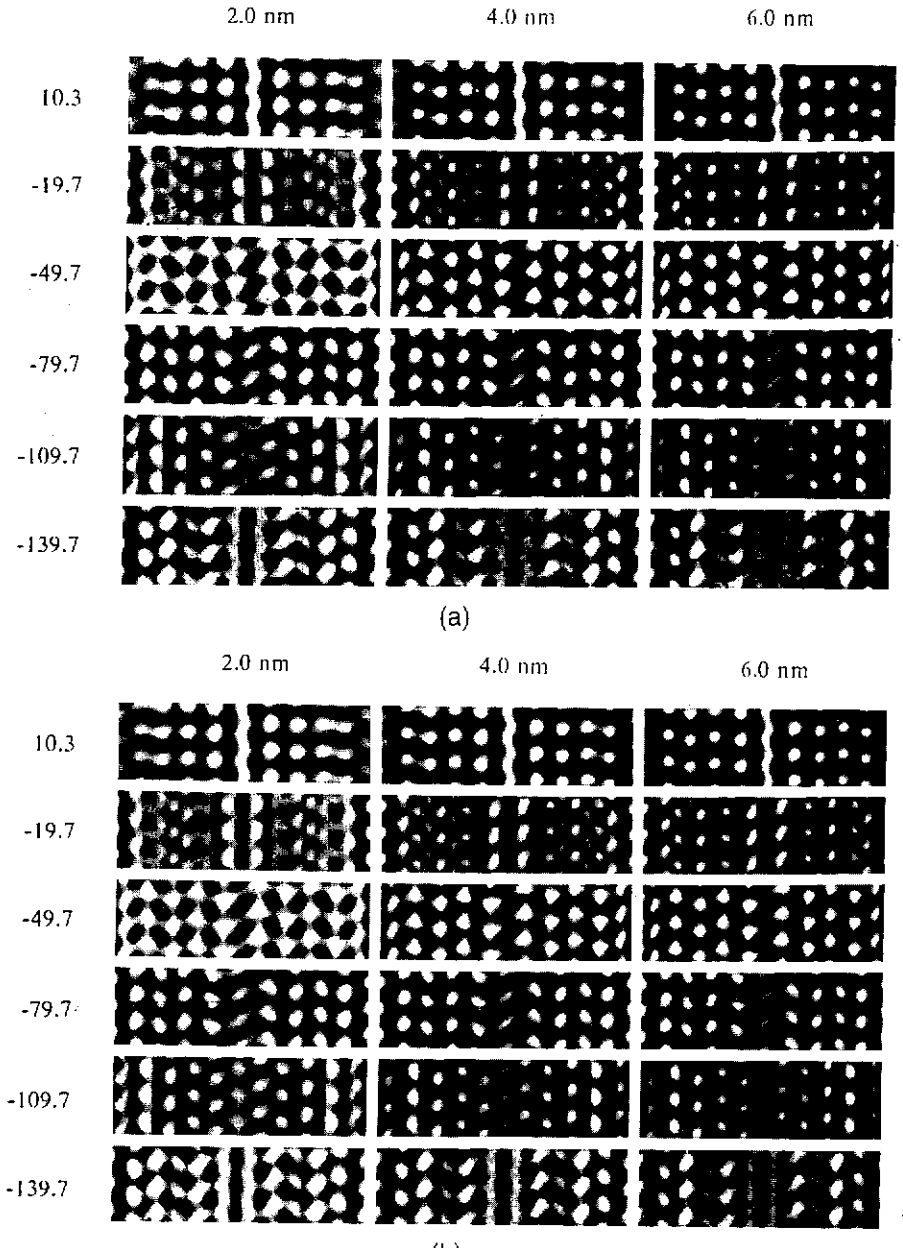


FIG. 9. Defocii and foil thickness montages for (a) the model of Harris *et al.* with $\mathbf{R} = 1/3\langle 10\bar{1}1\rangle$, and (b) the model containing the adjusted *c*-axis parameter with $\mathbf{R} = 1/3\langle 10\bar{1}0\rangle + 0.387\langle 0001\rangle$. No difference can be seen between the image characteristics of the two slightly different models.

oxygen impurity. The output from the program provided the oxygen, nitrogen, and aluminum x-ray intensities generated in the IDB and the AlN matrix. These intensities were converted into compositions by use of a *k*-factor.[65] The oxygen concentration of the IDB calculated for each of the eight models was determined for a foil thickness of 60 nm and 110 nm. These values of foil thickness were chosen to closely match the foil thickness of the experimentally determined data points, enabling comparisons to be made with the experimentally determined oxygen concentrations at the boundary. The oxygen concentrations determined by Monte Carlo simulation for each of the eight models are presented in Table III. Figure 12 shows a simulated profile using the planar IDB model proposed by Harris *et al.*[10,23] (model 6). The calculated profile is half the width of the experimental profile. This observed discrepancy, in the measured width of the oxygen profile from the IDB can be attributed either to a dilute oxygen cloud surrounding the planar IDB, or a slight misalignment of the boundary so that it was not exactly parallel to the beam.

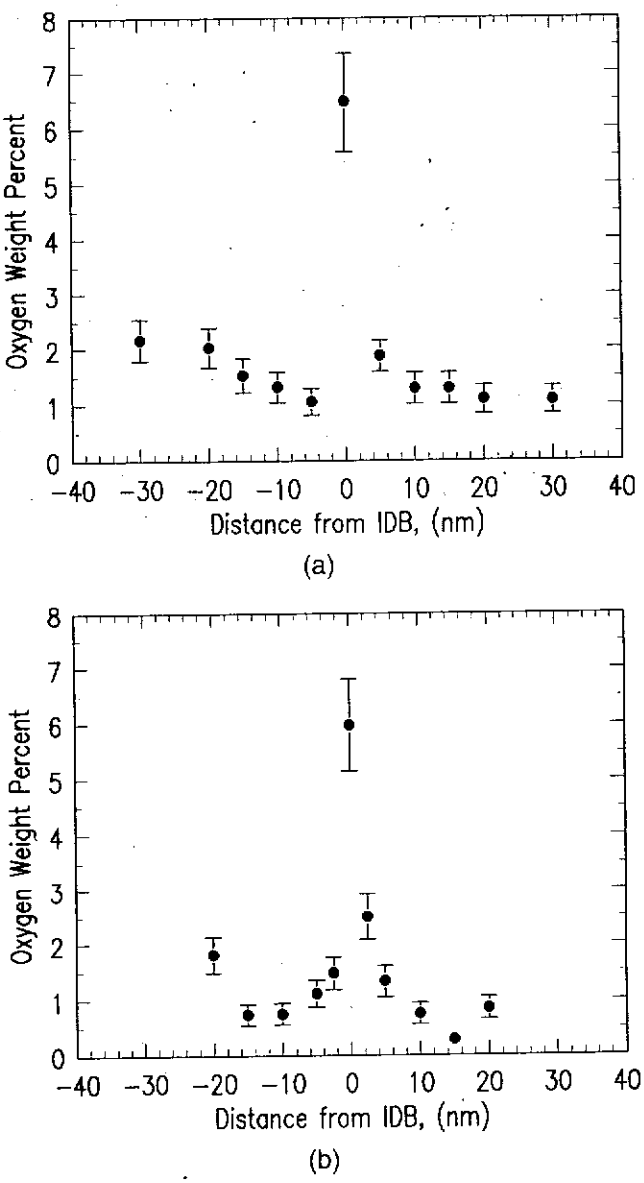


FIG. 10. (a,b) Quantitative oxygen concentration profiles form two different planar IDB's.

TABLE II. Experimentally determined oxygen concentrations for several planar IDB's.

| Oxygen weight % | Sample thickness (nm) |
|---|---|
| 6.5 ± 0.9 | 109 |
| 6.4 ± 0.9 | 106 |
| 5.0 ± 0.7 | 117 |
| 7.5 ± 1.0 | 103 |
| 6.0 ± 0.8 | 106 |
| 4.7 ± 0.7 | 103 |
| 6.0 ± 0.8 | 108 |
| 4.4 ± 0.7 | 101 |
| 7.8 ± 1.1 | 55 |

A comparison between the experimentally determined oxygen concentrations and the Monte Carlo simulations of the oxygen concentrations at the boundaries showed that model 6 and model 7 provided very good matches between the experimental and calculated values. The simulations of models 5 and 8 were to study the local oxygen environment around the octahedrally coordinated aluminum atom, in particular to determine whether the aluminum was coordinated only with oxygen, or three oxygen and one nitrogen, as suggested by Youngman,[45] whose argument was based upon maintaining charge neutrality at the interface. The simulations showed that an all-oxygen interface provided too high an oxygen content when compared with experiment. This suggests that the all-oxygen interface is not the preferred structure. Oxygen concentrations calculated for models 1, 2, and 3 were between one and four times higher than the experimentally measured oxygen concentrations. Model 4 had a slightly lower oxygen concentration than the experimentally measured value; its width was so small that based on the HRTEM studies this model was discounted.

Therefore, these AEM results are consistent with a planar IDB whose chemistry and structure can best be described as an octahedrally coordinated plane of aluminum sandwiched between two basal planes of substituted oxygen, with every fourth oxygen being replaced by a nitrogen. The experimentally determined oxygen concentration data are slightly higher than the calculated oxygen values. This can be understood if the actual oxygen concentration in the AlN matrix was higher than our assumed value of ≃1 wt.%.

### D. Atomistic computer simulations

Atomistic computer simulations have provided a means to probe the finer structural details of the planar

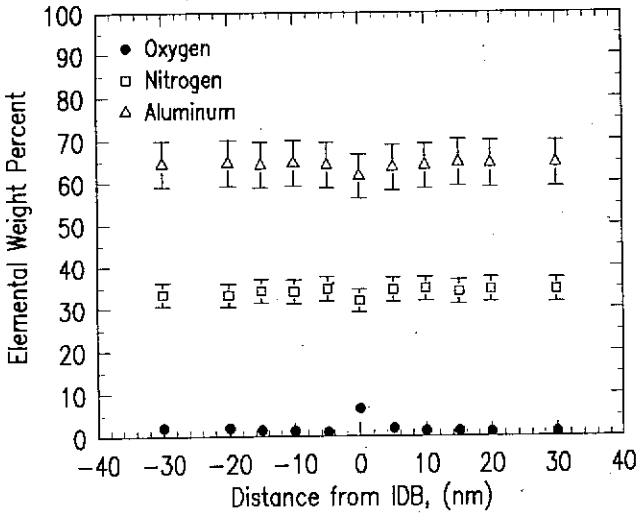


FIG. 11. Concentration profiles for aluminum, nitrogen, and oxygen from the planar IDB shown in Fig. 10(a).

TABLE III. Calculated oxygen concentrations using a Monte Carlo simulation for the eight proposed planar IDB models. The model of Youngman[45] and the model based on the experimental data presented here[59] are the best match with the experimental data. These data also support the argument that nitrogen is present at the planar IDB interface rather than pure alumina.

| Model | Boundary width (nm) | Composition | Calculated oxygen concentration | |
|---|---|---|---|---|
| | | | 110 nm | 600 nm |
| McKernan *et al.*[18] 1/3 unit cell of alumina | 0.433 | AlO | 12.8 | 14.8 |
| Westwood[59] (111) slab of AlON | 0.458 | AlON | 17.8 | 19.5 |
| Hagege *et al.*[12] **R** = 1/3⟨10$\bar{1}$0⟩ + 0.35⟨0001⟩ | 0.174 | $Al_2O_3$ | 9.0 | 10.4 |
| Hagege and Ishida[20] **R** = 1/3⟨10$\bar{1}$0⟩ + 0.15⟨0001⟩ | 0.075 | $Al_2O_3$ | 5.0 | 5.8 |
| Harris *et al.*[10] and McCartney *et al.*[23] **R** = 1/3⟨10$\bar{1}$0⟩ + 0.333⟨0001⟩ | 0.165 | $Al_2O_3$ | 9.3 | 10.9 |
| Youngman[45] IDB **R** = 1/3⟨10$\bar{1}$0⟩ + 0.333⟨0001⟩ | 0.165 | $Al_3O_3N$ | 6.7 | 7.7 |
| Westwood[59] IDB **R** = 1/3⟨10$\bar{1}$0⟩ + 0.387⟨0001⟩ | 0.192 | $Al_3O_3N$ | 7.1 | 8.1 |
| Westwood[59] IDB **R** = 1/3⟨10$\bar{1}$0⟩ + 0.387⟨0001⟩ | 0.192 | $Al_2O_3$ | 8.2 | 9.5 |

IDB: the effect of aluminum vacancies, the number of oxygen atoms around the octahedrally coordinated aluminum, and possibly to confirm the experimentally measured *c*-axis displacement of 0.387⟨0001⟩.

A large number of supercells were constructed, each containing a different IDB structure and chemistry. The energies of each of the different supercells were calculated, then compared against each other, and also against the theoretical energy of the supercell structure in order to determine their relative stability. Initially, pure IDB's comprised of all Al–Al or N–N bonds across the basal plane interface [as shown in Fig. 2(b)] with no oxygen and without the introduction of a translation were studied. The program was unable to find an equilibrium minimum energy configuration for these structures, indicating that this type II IDB interface is highly unstable, and the likelihood of its existence would be small. This result agrees with the antisite energy values for this type of interface based upon Van Vechten's[33] approach (see Table I) where an AlN (0001) IDB interface would have a large energy of 12.9 $Jm^{-2}$.

Models comprised of octahedrally coordinated aluminum, surrounded by nitrogen, and incorporating a translation were next considered, and minimum energy equilibrium structures were found. However, the energy changes $\Delta E$ were positive which indicates that these would not be stable configurations. However, the replacement of nitrogen with oxygen at the interface provided a dramatic improvement in stability, going from a positive to a negative $\Delta E$. This indicates that incorporating the oxygen within the planar defect is energetically more favorable than having it randomly distributed through the structure. This structural configuration was found to be most energetically favorable when oxygen atoms occupied three out of four nitrogen sites at the interface. These atomistic calculations therefore confirm the TEM and AEM results, and support the conclusion that these defects require oxygen to stabilize the interface.

Evaluation of the *c*-axis component of the displacement vector was conducted in two ways. First, in the minimization process, the lattice vectors of the supercell are allowed to vary, so that any relaxation across the interface (both perpendicular to the *c*-axis and parallel to the *c*-axis) will automatically result in a displacement which can be compared with experiment. Second, the initial magnitude of the *c*-axis displacement across the interface was varied from 0.11⟨0001⟩ to 0.61⟨0001⟩ (and relaxation allowed). In both cases, the structure and the displacement across the interface after energy minimization was always found to be the same, independent of the starting input.

The equilibrium structure of the planar IDB that was consistently output is shown in Fig. 13. Two structurally important observations can be made: first, the oxygen-nitrogen mixed basal plane on either side of the octahedrally coordinated aluminum IDB plane is not perfectly planar, and second, the distance of the adjacent

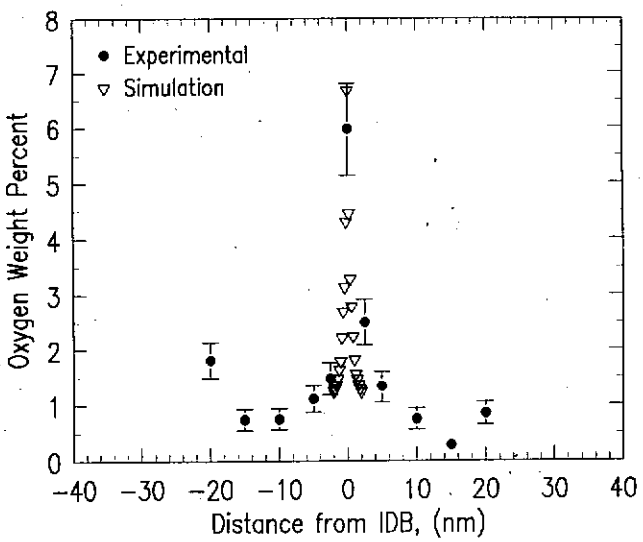


FIG. 12. A comparison of an experimental oxygen concentration profile [Fig. 10(b)] with a simulated oxygen profile using the model proposed by Harris *et al.*, with the basal planes adjacent to the octahedrally coordinated aluminum atoms having an oxygen nitrogen ratio of 3 : 1.

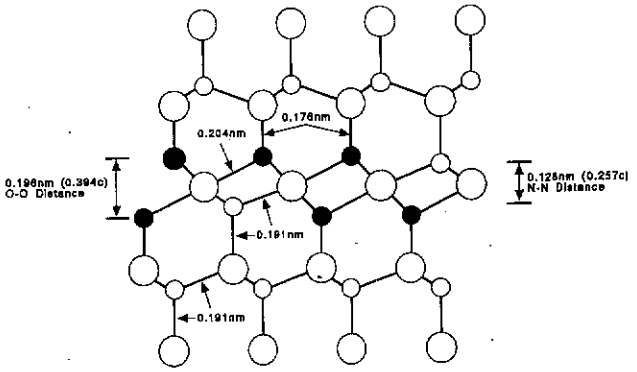


FIG. 13. A $\langle 11\bar{2}0 \rangle$ projection of the equilibrium IDB structure based upon the atomistic calculations. The large circles represent aluminum, the small dark circles are oxygen, and the small light gray circles are nitrogen. The various bond lengths are indicated, along with the oxygen-oxygen and nitrogen-nitrogen distances.

basal planes on either side of the IDB is shorter due to the influence of the tetrahedral Al–O bond (Al–O = 0.176 nm; Al–N = 0.191 nm). The distance between the oxygen atoms on either side of the boundary was calculated to be 0.394⟨0001⟩ (0.196 nm), and the distance between the nitrogen atoms was calculated as 0.257⟨0001⟩ (0.128 nm). The octahedral Al–O bond at the IDB interface is 0.204 nm, and the Al–N bond is 0.191 nm; the difference is due to the varying *c*-axis displacement of the oxygen and nitrogen atoms from the central aluminum IDB plane. The difference between the tetrahedral Al–O bond adjacent to the IDB and the octahedral Al–O bond at the IDB is believed to be due to the repulsive influence of the nitrogen displacing the oxygen atoms on either side of the IDB away from the central aluminum plane, resulting in an increased bond length.

A difficult question arises when trying to quantify the displacement vector across the boundary because of the "puckered" basal plane structure on either side of the octahedral aluminum plane. Three possible values are available based upon the calculations: a simple weighted average of the oxygen-oxygen and nitrogen-nitrogen distances results in $\mathbf{R} = 0.358\langle 0001 \rangle$, the oxygen-oxygen distance provides $\mathbf{R} = 0.394\langle 0001 \rangle$, and lastly, taking only the nitrogen-nitrogen distances gives $\mathbf{R} = 0.257\langle 0001 \rangle$. However, the last case can be ruled out because the distance is much less than observed in the experimental images. The two remaining values for the displacement vector are both in good agreement with the experimentally measured value.

Changing the oxygen content at the interface had the effect of adjusting the equilibrium *c*-axis displacement. When the interface was comprised of all oxygen with no nitrogen being present, the *c*-axis displacement was found to be 0.333⟨0001⟩, as suggested by Harris *et al.*[10] However, this interface was less stable than the interface structure that consisted of three oxygen and one nitrogen and a *c*-axis displacement of 0.358⟨0001⟩. This observation indicates that the chemistry of the interface is the primary controlling factor determining the equilibrium interface structure, and further that the composition suggested by Westwood *et al.*[22] is correct.

The role of aluminum vacancies on the interface structure was also investigated. The calculations indicated that incorporation of aluminum vacancies at the octahedral aluminum sites (center of the IDB) or adjacent to the oxygen-rich basal planes was not favorable. Therefore, aluminum vacancies may be considered to be repelled from the planar IDB interface.

Some degree of distortion on one side of the interface was observed, which appeared to indicate a twist, supporting the CBED results and the HRTEM observations of McCartney *et al.*[23] This twist was lost on moving away from the interface. This is probably due to a small amount of strain being present at the interface, possibly resulting in part from the distortion in the octahedral structural unit due to the presence of nitrogen.

The *c*-axis displacement across the IDB obtained from the atomistic calculations, 0.358⟨0001⟩, matches reasonably well with the weak-beam measured value of 0.387⟨0001⟩. Interestingly, these values are both very close to the *u* parameter value for AlN, 0.3821(3), reported by Schulz and Thiemann,[69] and 0.385 reported by Jeffery and Parry.[70] The *u* parameter is a measure of the Al–N separation along the *c*-axis in the wurtzite structure and expressed as a ratio of the *c*-axis. The similarity between the interface displacement and an important crystal structure property may also have an influence on the final interface structure, since this would

minimize distortions within the crystal, thus minimizing the overall energy of the system.

Finally, in an attempt to determine between displacements in the $c$-axis of $0.358\langle 0001\rangle$ and $0.394\langle 0001\rangle$, supercells were constructed for HRTEM image simulations containing structures with displacement vectors of $\mathbf{R} = 1/3\langle 10\bar{1}0\rangle + 0.358\langle 0001\rangle$ and $\mathbf{R} = 1/3\langle 10\bar{1}0\rangle + 0.394\langle 0001\rangle$. Both models contained the relaxation in atomic spacing on either side of the IDB due to the shorter Al–O bond lengths. An almost perfect match between the experimental image and simulated image was achieved with $\mathbf{R} = 1/3\langle 10\bar{1}0\rangle + 0.394\langle 0001\rangle$ as shown in Fig. 14(a). Figure 14(b) shows the match between the experimental and calculated intensities across the IDB; perfect registry between the atomic planes is achieved with this model. Therefore, the displacement vector for the planar IDB is $\mathbf{R} = 1/3\langle 10\bar{1}0\rangle + 0.394\langle 0001\rangle$.

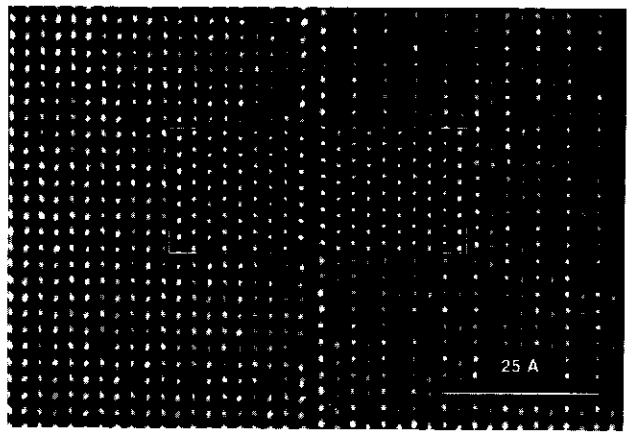


(a)

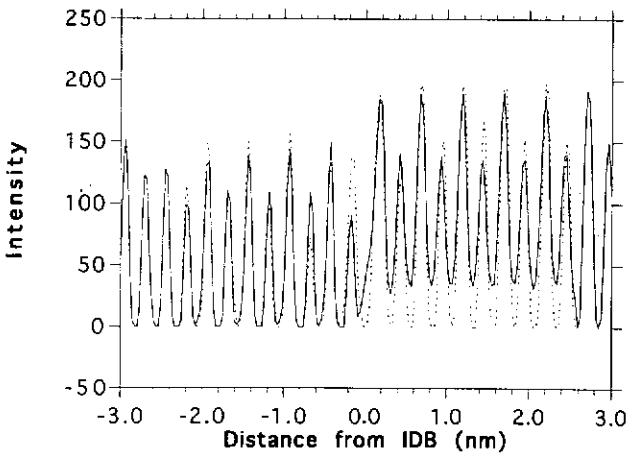


(b)

FIG. 14. (a) An experimental image of the planar IDB, with a simulated image of the interface structure superimposed across the boundary. The simulation image was constructed based upon the calculated structure and with $\mathbf{R} = 1/3\langle 10\bar{1}0\rangle + 0.394\langle 0001\rangle$ and with the relaxation due to the short Al–O bonds adjacent to the interface. (b) A plot of experimental (dashed line) and calculated intensity (solid line) based on the model versus distance on either side of the IDB; the excellent match can clearly be seen supporting the conclusions regarding the structure, displacement vector, and chemistry of the planar IDB.

## IV. CONCLUSIONS

The planar boundaries observed in oxygen-containing AlN are inversion domain boundaries (IDB's). These interfaces require the presence of oxygen for them to be stable in the AlN matrix. The interface is comprised of a basal plane of aluminum atoms, octahedrally coordinated to oxygen and nitrogen atoms in the ratio of 3 to 1. This was verified by HRTEM, AEM, and atomistic calculations. The displacement vector for the interface has been measured experimentally, and was found to be $\mathbf{R} = 1/3\langle 10\bar{1}0\rangle + 0.387\langle 0001\rangle$. Atomistic computer simulations verified the interface structure and chemistry and determined the displacement vector to be $\mathbf{R} = 1/3\langle 10\bar{1}0\rangle + 0.394\langle 0001\rangle$. This result is in good agreement with the experimental results. The calculations also revealed a contraction of the basal interplanar spacing on either side of the IDB due to the Al–O bond, aluminum vacancies were repelled from the interface, and that a distortion in the form of a twist was present on one side of the interface, supporting the HRTEM and CBED observations.

These results reaffirm the importance of chemistry as a controlling factor in defect formation, and also the host crystal structure, in which the defect is expected to sit. The role of chemistry is emphasized by the observations and calculations which indicate the requirement for impurities to be present to allow the formation of IDB's.

## ACKNOWLEDGMENTS

The authors wish to thank the Semiconductor Research Corporation (SRC) and British Petroleum America for funding this work, Dr. J. R. Michael for assistance with the Monte Carlo simulations, Dr. S. Witek for supplying the undoped hot pressed AlN sample, and the external users program at the Center for High-Resolution Electron Microscopy at Arizona State University.

## REFERENCES

1. L. C. Otero-Diaz and B. G. Hyde, Acta Crystallogr. B **40**, 237–244 (1984).
2. M. G. Blanchin, L. A: Bursill, and D. J. Smith, Proc. R. Soc. London A **391**, 351–372 (1984).
3. L. Kihlborg and R. Sharma, J. Microsc. Spectrosc. Electron. **7**, 387 (1982).
4. M. Lundberg, M. Sundberg, and A. Magneli, J. Solid State Chem. **44**, 32–40 (1982).
5. P. J. England and R. J. D. Tilley, Chem. Scripta **22**, 108 (1983).
6. S. Hagege, Y. Ishida, and S. Tanaka, ISE Grain Boundary Meeting, July 1987, Lake Placid, NY (1987).
7. A. D. Westwood and M. R. Notis, Adv. Ceram. **26**, 171–187 (1989).
8. J. C. Kim and E. Goo, J. Am. Ceram. Soc. **73**, 877–884 (1990).

9. A. D. Westwood, R. A. Youngman, M. R. McCartney, A. N. Cormack, and M. R. Notis, J. Mater. Res. **10**, 1287–1300 (1995).
10. J. H. Harris, R. A. Youngman, and R. G. Teller, J. Mater. Res. **5**, 1763–1773 (1990).
11. S. Hagege, S. Tanaka, and Y. Ishida, J. Phys. (Paris) **49**, C5, 189–194 (1988).
12. S. Hagege, S. Tanaka, and Y. Ishida, J. Jpn. Inst. Metals **52**, 1192–1198 (1988).
13. R. A. Youngman, in *Proc. 46th EMSA Meeting*, Milwaukee, WI, edited by G. W. Bailey (San Francisco Press, San Francisco, CA, 1988), pp. 576–577.
14. M. F. Denanot and J. Rabier, J. Mater. Sci. **24**, 1594–1598 (1989).
15. S. McKernan and C. B. Carter, in *Advanced Electronic Packaging Materials*, edited by A. T. Barfknecht, J. P. Partridge, C. J. Chen, and C-Y. Li (Mater. Res. Soc. Symp. Proc. **167**, Pittsburgh, PA, 1989), pp. 289–294.
16. A. D. Westwood and M. R. Notis, in *Advanced Electronic Packaging Materials*, edited by A. T. Barfknecht, J. P. Partridge, C. J. Chen, and C-Y. Li (Mater. Res. Soc. Symp. Proc. **167**, Pittsburgh, PA, 1989), pp. 295–300.
17. R. A. Youngman, J. H. Harris, P. A. Labun, R. J. Graham, and J. K. Weiss, in *Advanced Electronic Packaging Materials*, edited by A. T. Barfknecht, J. P. Partridge, C. J. Chen, and C-Y. Li (Mater. Res. Soc. Symp. Proc. **167**, Pittsburgh, PA, 1989), pp. 301–306.
18. S. McKernan, M. G. Norton, and C. B. Carter, in *High-Resolution Electron Microscopy of Defects in Materials*, edited by R. Sinclair, D. J. Smith, and U. Dahmen (Mater. Res. Soc. Symp. Proc. **183**, Pittsburgh, PA, 1990), pp. 267–272.
19. A. Berger, J. Am. Ceram. Soc. **74**, 1148–1151 (1991).
20. S. Hagege and Y. Ishida, Philos. Mag. A **63**, 241–258 (1991).
21. A. D. Westwood and M. R. Notis, J. Am. Ceram. Soc. **74**, 1226–1239 (1991).
22. A. D. Westwood, J. R. Michael, and M. R. Notis, in *Microbeam Analysis 1991*, edited by D. G. Howitt (San Francisco Press, San Francisco, CA, 1991), pp. 245–249.
23. M. R. McCartney, R. A. Youngman, and R. G. Teller, Ultramicrosc. **40**, 291–299 (1992).
24. A. D. Westwood, J. R. Michael, and M. R. Notis, J. Microsc. **167**, 287–302 (1992).
25. G. A. Slack, J. Phys. Chem. Solids **34**, 321–335 (1973).
26. J. Tafto and J. C. H. Spence, J. Appl. Crystallogr. **15**, 60–64 (1982).
27. M. Snykers, R. Serneels, P. Delavignette, G. Gevers, J. Van Landuyt, and S. Amelinckx, Phys. Status Solidi A **41**, 51–63 (1977).
28. G. Aminoff and G. Broome, Kristallogr. Kristallgeom. Krystallphys. Kristallchem. **80**, 355–376 (1931).
29. S. B. Austerman and W. G. Gehman, J. Mater. Sci. **1**, 249–260 (1966).
30. D. B. Holt, J. Phys. Chem. Solids **30**, 1297–1308 (1969).
31. P. Pirouz, C. M. Chorey, and J. A. Powell, J. Appl. Phys. Lett. **50**, 221–223 (1987).
32. Z. Liliental-Weber, M. A. O'Keefe, and J. Washburn, Ultramicrosc. **30**, 26–30 (1989).
33. J. A. Van Vechten, J. Electrochem. Soc. **22**, 423–429 (1975).
34. O. Unal and T. E. Mitchell, J. Mater. Res. **7**, 1445–1454 (1992).
35. W. R. L. Lambrecht and B. Segall, Phys. Rev. B **41**, 2948–2958 (1990).
36. V. P. Dravid, Ph.D. Dissertation, Lehigh University, Bethlehem, PA (1990).
37. W. C. Mackrodt, in *Structure and Properties of MgO and $Al_2O_3$ Ceramics*, edited by W. D. Kingery (The American Ceramics Society, Inc., Westerville, OH); Adv. Ceram. **10**, 271–280 (1984).
38. D. Wolf, in *Structure and Properties of MgO and $Al_2O_3$ Ceramics*, edited by W. D. Kingery (The American Ceramics Society, Inc., Westerville, OH); Adv. Ceram. **10**, 290–302 (1984).
39. D. M. Duffy and P. W. Tasker, in *Structure and Properties of MgO and $Al_2O_3$ Ceramics*, edited by W. D. Kingery (The American Ceramics Society, Inc., Westerville, OH); Adv. Ceram. **10**, 281–289 (1984).
40. L. Pauling, *The Nature of the Chemical Bond* (Cornell University Press, Ithaca, NY, 1960), pp. 64–107.
41. D. Makovec and M. Trontelj, J. Am. Ceram. Soc. **77**, 1202–1208 (1994).
42. J. Bruley, U. Bremer, and V. Krasevec, J. Am. Ceram. Soc. **75**, 3127–3128 (1992).
43. J. C. Kim and E. Goo, J. Mater. Sci. **24**, 76–82 (1989).
44. O. Massler, K-U. Senftleben, and H. G. Sockel, Mater. Sci. Eng. A **154**, L19–L24 (1992).
45. R. A. Youngman, private communication (1990).
46. P. A. Stadelmann, Ultramicrosc. **21**, 131–145 (1987).
47. J. R. Michael, D. B. Williams, C. F. Klein, and R. Ayer, J. Microsc. **160**, 41–53 (1989).
48. T. Malis, S. C. Cheng, and R. F. Egerton, J. Electron Microsc. Tech. **8**, 193–200, (1988).
49. A. N. Cormack, Adv. Solid State Chem. **3**, 63–98 (1993).
50. A. N. Cormack, J. Am. Ceram. Soc. **72**, 1730–1732 (1989).
51. J. C. Philips, Phys. Rev. Lett. **20**, 550–553 (1968).
52. J. A. Van Vechten, Phys. Rev. B **182**, 891–905 (1969).
53. W. C. Mackrodt and R. F. Stewart, J. Phys. C; Solid State Phys. **12**, 431–449 (1979).
54. G. V. Lewis and C. R. A. Catlow, J. Phys. C; Solid State Phys. **18**, 1149 (1985).
55. P. W. Tasker and T. J. Bullough, Philos. Mag. A **43**, 313–324 (1981).
56. C. R. A. Catlow and W. C. Mackrodt, in *Computer Simulation of Solids*, edited by C. R. A. Catlow and W. C. Mackrodt (Springer-Verlag, New York, 1982), pp. 3–20.
57. A. N. Cormack and C. R. A. Catlow, in *Atomic Scale Calculations in Materials Science*, edited by J. Tersoff, D. Vanderbilt, and V. Vitek (Mater. Res. Soc. Symp. Proc. **141**, Pittsburgh, PA, 1989), pp. 65–70.
58. A. N. Cormack, R. M. Jones, P. W. Tasker, and C. R. A. Catlow, J. Solid State Chem. **44**, 174–185 (1982).
59. A. D. Westwood, Ph.D. Dissertation, Lehigh University, Bethlehem, PA (1992).
60. K. Miyazawa and Y. Ishida, Ultramicrosc. **22**, 231–238 (1987).
61. K. Miyazawa, Y. Ishida, and T. Suga, Philos. Mag. A **58**, 825–832 (1988).
62. D. J. H. Cockayne, J. Microsc. **98**, 116–134 (1973).
63. D. R. Rasmussen and C. B. Carter, J. Electron Microsc. Tech. **18**, 429–436 (1989).
64. D. R. Rasmussen, N. Cho, D. W. Susnitzky, and C. B. Carter, Ultramicrosc. **30**, 27–32 (1989).
65. W. O. Saxton and D. J. Smith, Ultramicrosc. **18**, 39–49 (1985).
66. D. F. Kyser, in *Introduction to Analytical Electron Microscopy*, edited by J. J. Hren, J. I. Goldstein, and D. C. Joy (Plenum Press, New York, 1979), pp. 199–219.
67. A. D. Romig, S. J. Plimpton, J. R. Michael, R. L. Myklebust, and D. E. Newbury, in *Microbeam Analysis 1990*, edited by J. R. Michael and P. Ingram (San Francisco Press, San Francisco, CA, 1990), pp. 275–279.
68. G. Cliff and G. W. Lorimer, J. Microsc. **103**, 203–207 (1975).
69. H. Schultz and K. H. Thiemann, Solid State Commun. **23**, 815–819 (1977).
70. G. A. Jeffery and G. S. Parry, J. Chem. Phys. **23**, 406 (1955).